JOURNAL OF GEOPHYSICAL RESEARCH, VOL. 98, NO. A9, PAGES 15,553–15,559, SEPTEMBER 1, 1993

The Scattering of VLF Waves by Localized Ionospheric Disturbances Produced by Lightning-Induced Electron Precipitation

WILLIAM L. POULSEN,[1] TIMOTHY F. BELL, AND UMRAN S. INAN

Space, Telecommunications and Radioscience Laboratory, Stanford University, Stanford, California

A three-dimensional model of the scattering of VLF waves in the Earth-ionosphere waveguide by localized disturbances in the lower ionosphere is examined for typical disturbances expected to be produced by lightning-induced electron precipitation events. Results indicate that the scattering is generally independent of the conductivity and permittivity of the Earth's surface immediately beneath the disturbed region except for extremely low conductivities such as that found over deep ice caps. Thus the scattered signal is principally a function of the ionospheric perturbation. For typical disturbances characterized by altitude profiles of enhanced ionization expected for $1.4 \leq L \leq 3$, most of the measurable wave energy scatters within a fairly narrow angular region (15-dB beam width of $\pm 7°$ for a disturbance radius of 100 km) centered on the forward scatter direction. Thus moderate- to large-scale disturbances (radius 50-200 km) must be located within <250 km of a moderate-length path (3000-16,000 km) in order to scatter a measurable signal to the receiver. These two findings suggest that the scattered signals can be used with confidence as a diagnostic tool to determine the characteristics of the energetic electron precipitation.

1. INTRODUCTION

Subionospheric VLF probing has recently emerged as a powerful tool for remote sensing of transient ionospheric perturbations associated with lightning-generated whistlers [*Inan and Carpenter,* 1987; *Inan et al.,* 1988*b*] or lightning discharges [*Inan et al.,* 1988*b*; *Yip et al.,* 1991]. The phenomenon is sometimes referred to as the "Trimpi" effect, in which phase and/or amplitude perturbations in subionospheric VLF radio signals occur in response to secondary ionization generated in the lower ionosphere by lightning-induced electron precipitation bursts [*Helliwell et al.,* 1973; *Lohrey and Kaiser,* 1979; *Dowden and Adams,* 1988, 1989*a*, *b*, 1990; *Cotton and Smith,* 1991] (see Figure 1*a*). In general, these perturbations are observed only during the night, when the reflection height for VLF waves in the *D* region lies above the region of secondary ionization.

Quantitative interpretation and understanding of lightning-associated VLF perturbation events must be based on a model of subionospheric VLF propagation in the presence of localized density enhancements in the nighttime *D* region. In particular, a three-dimensional model is needed, since the disturbances are likely to be of finite transverse extent and can be located off the great circle path (GCP). Such a model was recently proposed by *Poulsen et al.* [1990*a*].

In principle, a three-dimensional model of the scattering process can be used as a diagnostic tool to determine the magnitude of the energetic electron precipitation flux and the location of the perturbed region of the ionosphere. In practice, the usefulness of this tool would be enhanced if the characteristics of the scattered signal did not depend significantly upon the conductivity of the Earth immediately beneath the perturbed ionospheric region but instead were a function primarily of the ionospheric perturbation. In order to locate the perturbation from multiple VLF path measurements [*Inan et al.,* 1990], it would also be useful to be able to set an upper bound on the transverse displacement of the perturbed region from the GCP between transmitter and receiver.

In the present paper we address two questions. The first concerns the effect of the ambient ground conductivity on the amplitude and phase of the signal scattered by the ionospheric disturbance. The second concerns the beam width of the scattered signal as a function of the characteristics of the input mode, a quantity which determines the maximum displacement of the perturbed region from the GCP.

2. DESCRIPTION OF THE SCATTERING MODEL

Figure 1 shows the basic geometry of the 3-D scattering problem. With this model, *Poulsen et al.* [1990*a*] derived an expression for the scattered modal field e_n^s observed at the receiver in terms of the unperturbed modal field e_n^o that would be observed at the receiver in the absence of any disturbance:

$$\left.\frac{e_n^s}{e_n^o}\right|_{(x_R,0)} \simeq \frac{-ik_o^2}{4}\sqrt{\frac{i2d}{\pi k_o S_n^o}} \int_0^{2\pi}\int_0^a \frac{[S_n^2(r') - (S_n^o)^2]}{\sqrt{R_o R'}} e^{-ik_o S_n^o (R_o + R' - d)} r' dr' d\theta' \quad (1)$$

where r' and θ' are polar coordinates within the perturbed region, d is the GCP distance between the transmitter and receiver, k_o is the free space wave number, $S_n(r')$ is the complex index of refraction along the direction of propagation, S_n^o is the ambient value of S_n in the absence of any disturbance (in the single-mode analysis, it is a constant independent of r' and θ'), and $\mathcal{P}$ (the region of integration) extends over that portion of the x-y plane that encompasses the disturbance (i.e., where $S_n \neq S_n^o$). The remaining variables are defined in Figure 1. For the purpose of this study, the region $\mathcal{P}$ is assumed to be a circular, cylindrically symmetric disturbance with effective radius a. In deriving (1), it is assumed that each modal field satisfies the Wentzel-Kramers-Brillouin (WKB) approximation within the perturbed region.

For a circular disturbance of the ionosphere of radius a located at (x_o, y_o) and for a given wave frequency, a complex value for

[1]Now at Jet Propulsion Laboratory, Pasadena, California.

Paper number 93JA01201.
0148-0227/93/93JA-01201$05.00

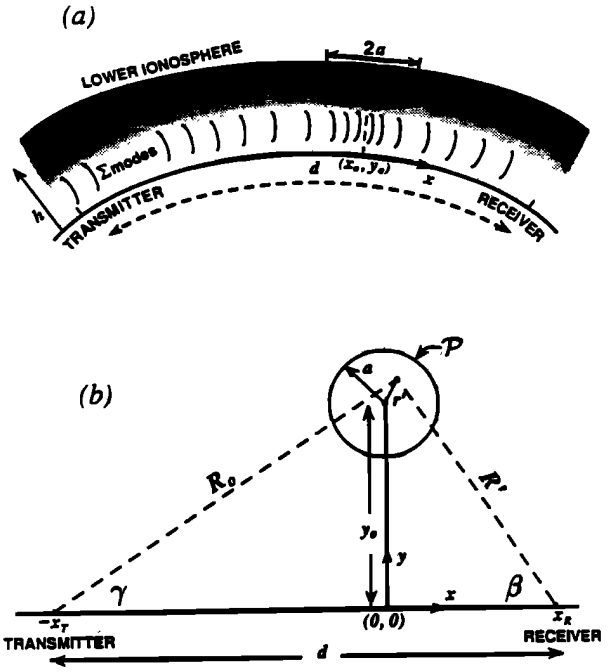

Fig. 1. (*a*) Cross-sectional view of the Earth-ionosphere waveguide between a transmitter and receiver separated by a distance d along the surface of the Earth. The change in the electron density with altitude h of the lower ionosphere is represented by the change in shading density. Also represented is a density enhancement perturbation of the ambient ionosphere such as those generated by lightning-induced electron precipitation bursts. The center of this disturbance is located at the point (x_o, y_o). Such a disturbance, appearing transiently, scatters some of the signal impinging on it and causes a temporary perturbation in the total signal measured at the receiver. (*b*) A plan view, seen from above, of the situation depicted in Figure 1*a* showing the three-dimensional configuration of the problem and identifying the geometry and variables used in the text. Note that the origin has been shifted to the point $x=x_o$.

the field scattered by the disturbance (relative to the "direct" signal) can be determined numerically from (1) if the ambient refractive index S_n^o and the refractive index in the disturbance region $S_n(r')$ are known. The equations given above provide a means to numerically model the effects of localized three-dimensional disturbances on VLF waves propagating in the Earth-ionosphere waveguide [*Poulsen et al.*, 1990*a*].

The complex quantities S_n and S_n^o can be computed using the mode theory of VLF propagation in the Earth-ionosphere waveguide [*Wait*, 1962]. In this theory the wave energy within the waveguide is considered to be partitioned among a series of waveguide modes. Each mode is associated with one of a discrete set of angles of incidence θ_n of the waves on the ionosphere for which constructive interference occurs and energy propagates away from the source. The complex quantities S_n and S_n^o are simply the (complex-valued) sine of the eigenangles θ_n (i.e., $S_n = \sin\theta_n$). The procedure for calculating the eigenangles is described by Poulsen et al. [1990*a*]. In general, the eigen-angles depend upon the reflective properties of both the ionosphere and the ground. However, for diagnostic purposes, (1) will be most useful if the values of S_n are determined predominantly by the ionospheric perturbation and are relatively independent of the ground conductivity.

3. Ionospheric Disturbances

One important cause of localized disturbances in the lower ionosphere, and the primary motivation behind the present work, is the precipitation of bursts of energetic electrons due to gyroresonance interactions in the magnetosphere between whistler waves from lightning and the energetic electrons [*Chang and Inan*, 1985]. When the energies of the precipitating electrons exceed ~50 keV, the particles penetrate down to altitudes below 90–100 km, where during the night they can alter the upper VLF waveguide boundary in a localized region and consequently affect the mode structure of the propagating waves [*Poulsen et al.*, 1990*a*].

Since the energy spectra of electrons precipitated by whistlers is a complicated function of wave frequency and magnetospheric parameters [*Chang and Inan*, 1985], a simple theoretical model developed by *Inan et al.* [1988*a*] has been used in past work [*Poulsen et al.*, 1990*b*, 1993] to estimate the modification of the lower ionospheric electron density profile that is expected to occur under different conditions. For the sake of comparison we will consider these same profiles in the present paper. The approximations and assumptions used in calculating the profiles are discussed by *Inan et al.* [1988*a*]. Figure 2 shows examples of several profiles (which we identify by the labels I, II, III, IV, and V) representative of the electron density at the location of maximum perturbation (x_o, y_o) as a function of altitude h resulting from electron precipitation bursts of 200-ms duration induced by lightning-generated whistlers propagating at L=3, 2.5, 2, 1.6, and 1.4, respectively, according to the *Inan et al.* [1988*a*] model. The ambient nighttime D region electron density profile, representative of geomagnetically quiet times, is also shown for reference. The total precipitating electron energy flux density for each profile was taken to be 1.5×10^{-2} ergs cm^{-2} s^{-1}.

The difference between the disturbed electron density $N_e(h)$ at the location of maximum ionospheric perturbation and the ambient nighttime density $N_e^o(h)$ is designated $\Delta N_e(h)$. The variation of $\Delta N_e(h)$ with distance in the horizontal direction r' (see Figure 1*b*) is represented in this work by a cylindrically symmetric Gaussian distribution such that

$$\Delta N_e(r', h) = \Delta N_e(x_o, y_o, h) e^{-(\frac{r'}{a})^2} \tag{2}$$

where $r' = [(x'-x_o)^2+(y'-y_o)^2]^{\frac{1}{2}}$ and the parameter a is the effective disturbance radius. In general, the refractive index $S_n(r')$ depends on density in a complex manner. However, analysis indicates that for the parameter ranges considered an approximate expression for $S_n(r')$ can be written

$$S_n(r') - S_n^o = [S_n(0) - S_n^o]\, e^{-(r'/a)^2} \tag{3}$$

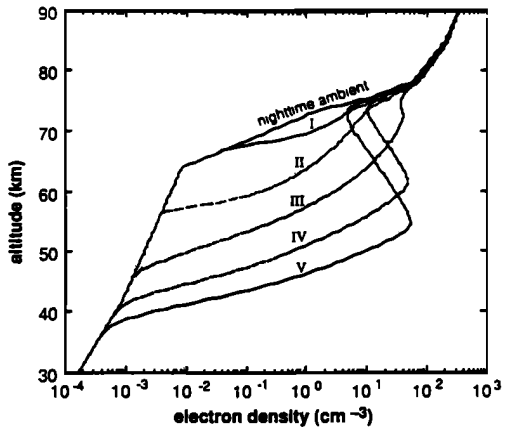

Fig. 2. Ionospheric profiles used for examples and comparisons in this work. See text for the rationale for selection of these profiles.

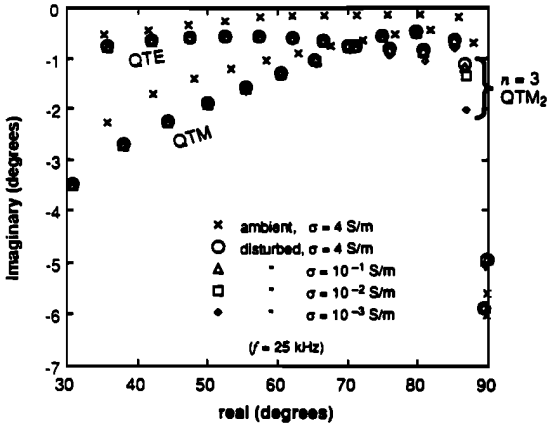

Fig. 3. Eigenangles for different surface conductivities. Wave frequency of 25 kHz and disturbed density enhancement profile II from Figure 2 were assumed. Eigenangles for both quasi-transverse electric (QTE) and quasi-transverse magnetic modes (QTM) are shown.

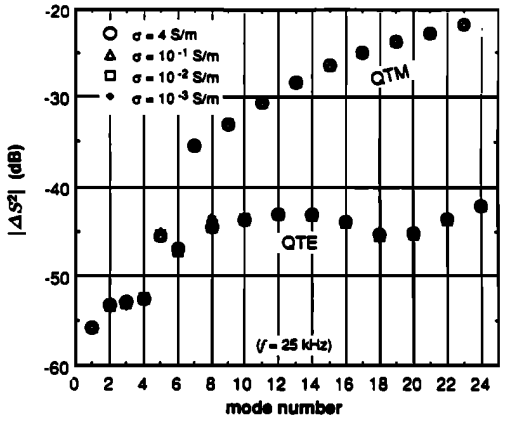

Fig. 4. ΔS^2 versus mode number for a 25-kHz signal, profile II of Figure 2, and for different surface conductivities as indicated.

4. Sensitivity of the Scattering to Surface Conductivity

Figure 3 is a plot of the eigenangle solutions [*Poulsen et al.*, 1990*a*] in the complex plane for a 25-kHz signal and with profile II of Figure 2 as the disturbed electron density profile for the lower ionosphere. The figure shows results for four different cases of Earth surface conductivity, ranging from $\sigma = 4$ S/m for seawater to $\sigma = 10^{-3}$ S/m for low-conductivity continental soil ($\epsilon_r = 81$ for the seawater case, and $\epsilon_r = 15$ for the other three cases). Also plotted are the eigenangle solutions for the ambient electron density profile of Figure 2 with $\sigma = 4$ S/m. The eigenangles are shown for both quasi-transverse electric (QTE) and quasi-transverse magnetic (QTM) modes.

Notice that the disturbed density eigenangle solutions for each mode are nearly identical regardless of the conductivity of the Earth surface boundary underneath the disturbed region. Only for mode $n = 3$ (QTM_2) is there any significant change in the eigenangle solution as the Earth surface conductivity is varied. The ambient ionosphere eigenangle solutions for Earth surface conductivities ranging from $\sigma = 10^{-1}$ to 10^{-3} S/m are also nearly identical to those of the ambient case shown in Figure 3 for $\sigma = 4$ S/m. This result indicates that the mode structure of propagating VLF waves encountering an ionospheric disturbance, as described by profile II of Figure 2, would be affected in a manner that is generally insensitive to differences in the conductivity σ of the surface under the disturbed region. In other words, a given ionospheric disturbance would scatter an incoming signal by the same amount whether the disturbance was over water or over different types of land.

Another way to illustrate this result is by plotting the difference term, $[S_n^2(r') - (S_n^o)^2]$ of (1), labeled ΔS^2 in Figure 4. This is the only part of (1) that depends on the properties of the disturbed region (i.e., the disturbed eigenangle solutions). As can be seen in the figure, the magnitude of ΔS^2 is nearly identical for all four ground conductivities for each mode. We note that since the strength of the scattered signal is directly proportional to the magnitude of ΔS^2 in (1), the larger the ΔS^2 difference term is, the larger the amplitude of the modal field scattered toward the receiver is. Also, since $S_n = \sin\theta_n$, the distance in the complex plane between an ambient-mode eigenangle solution and its corresponding disturbed-mode eigenangle solution gives a rough measure of the relative magnitude of the modal signal scattered towards the receiver by that disturbance. Thus the farther apart a given mode's ambient and disturbed eigenangle solutions are, the greater is the relative magnitude of the scattered field of that mode compared to that of modes whose ambient and disturbed eigenangle solutions are closer together in the complex-θ plane. Figure 3 indicates that for a 25-kHz signal, the higher-order QTM modes have larger scattered field strengths than the higher-order QTE modes for a disturbance having the electron density shown in profile II of Figure 3. However, we note that the overall effect of any mode on the total scattered field is also dependent on the relative strength of that mode which arrives at the disturbance, which in turn is a function of the amplitude of that mode initially excited at the transmitter and the attenuation it suffers before reaching the disturbance.

Although the results of Figures 3 and 4 strictly apply only for $f = 25$ kHz, additional calculations (not shown here) also demonstrate that over the entire frequency range 15 kHz $\leq f \leq$ 50 kHz the eigenangle solutions depend only weakly on ground conductivity when $\sigma \geq 10^{-3}$ s/m.

Finally, Figure 5 is for the same conditions as Figure 3 except that two additional sets of eigenangle solutions are plotted. One set is for a low Earth surface conductivity of $\sigma = 10^{-4}$ S/m and permittivity of $\epsilon_r = 10$, representative of ice shelves and shallow ice-covered ground. The other set is for a very low Earth surface conductivity of $\sigma = 10^{-5}$ S/m and permittivity of $\epsilon_r = 5$, representative of deep ice caps such as those in Greenland

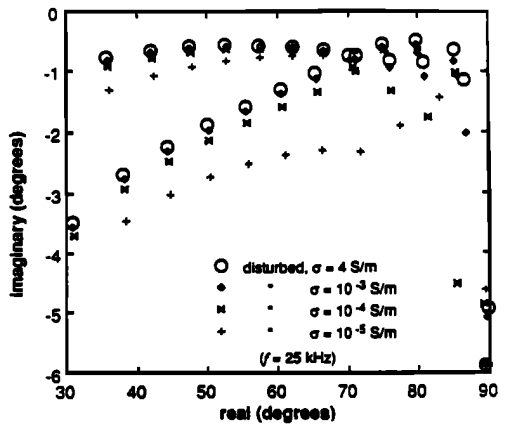

Fig. 5. Eigenangle solutions for ice cap surface conditions.

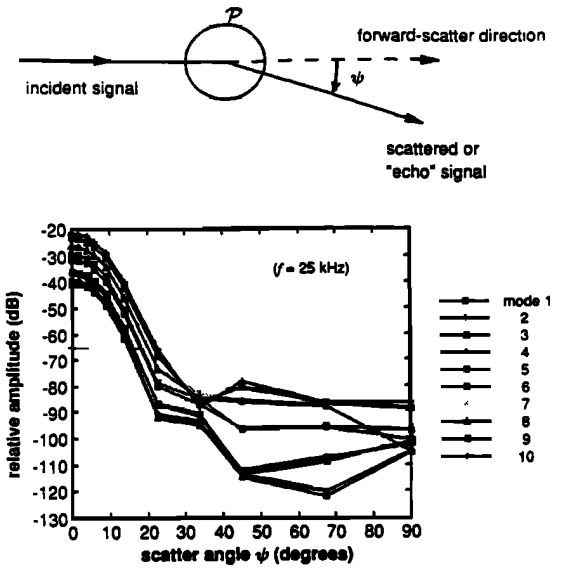

Fig. 6. (Top) Scattering geometry and definition of the angle ψ; (bottom) scattered modal signal strength versus angle ψ for a 25 kHz signal and a disturbance 50 km in radius. The density enhancement profile was assumed to be profile II from Figure 2, while the Earth surface conductivity and permittivity were taken to be σ = 4 S/m and ϵ_r=81.

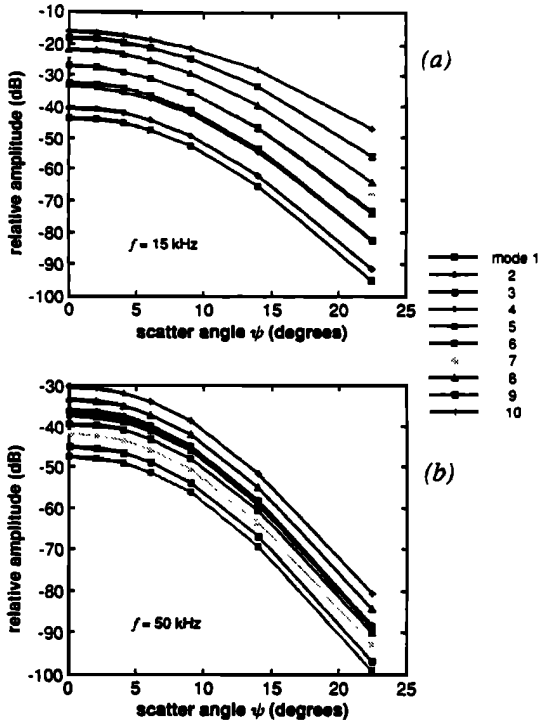

Fig. 7. Scattered signal "radiation" patterns for (*a*) 15-kHz signals and (*b*) 50-kHz signals. All other parameters are the same as in Figure 6.

and Antarctica [*Hauser et al.*, 1969]. For these conditions, and in particular over ice caps, the eigenangle solutions vary considerably from those described earlier in conjunction with Figure 3. Thus for propagation over these regions of the Earth, the scattering from disturbances with altitude profiles such as those shown in Figure 2 can be a sensitive function of the conductivity of the ground beneath the disturbance.

5. Beam Width of Scattered Wave Radiation Pattern

Another important property of the type of scatterers defined by the altitude profiles of Figure 2 and having a transverse extent of 50-200 km is their radiation pattern. Figure 6*b* shows a plot of the relative scattered signal strength calculated for each of the first 10 most significant modes of a 25-kHz signal as a function of the angle ψ (as depicted in Figure 6*a*) measured away from the forward scatter direction. The scattering region used in the case shown was chosen to have a disturbed electron density profile labeled II in Figure 2 at its center, with density falling off with distance from the center in the manner described by (3). The scattering region was assumed to have an effective radius a of 50 km, while the Earth surface conductivity and permittivity under the disturbance were respectively taken to be σ = 4 S/m and ϵ_r = 81.

Notice that the main lobe of the scattered "radiation" pattern extends out to $\psi \sim 20^\circ$ and is very similar (nearly identical) for every mode. Only the overall relative magnitude varies among the modes. The amplitudes of all the modes for scatter angles ψ outside the main lobe beam width are found to be uniformly much lower than the main lobe amplitudes for every non negligible waveguide mode over the entire range of frequencies (15–50 kHz), effective radii (25–200 km), disturbed density profiles (profiles I-IV of Figure 3), and ground conductivities (10^{-3}–4 S/m) considered. In all the cases involving the Gaussian-shaped disturbances considered in this work, only one main lobe is found, as depicted in Figure 6. Figures 7*a* and 7*b* show the results of calculations for the same conditions as those of Figure 6 but for frequencies of 15 and 50 kHz, respectively. The general form of the main lobe is seen to be very similar at all three frequencies. Experimental observations [*Carpenter et al.*, 1984; *Wolf and Inan*, 1990] indicate that typical normalized amplitudes (e_n^s/e_n^0) for signals scattered by ionospheric perturbations lie in the range 0.3-1 dB and that the noise threshold is roughly 0.04 dB. Thus, typically, the signal-to-noise ratio of the scattered signal was in the range 8-15 dB. This result suggests that the measurable beam width of the signal scattered from the ionospheric perturbation would be roughly given by twice the angle $|\psi| = \psi_{15}$ at which the radiation intensity is reduced 15 dB below that of the forward scatter direction $\psi = 0$. Adopting this definition of beam width, it can be seen from Figure 6 that $\psi_{15} \cong 12^\circ$.

Figure 8 compares the main lobe of the scattered radiation patterns of four different disturbances with transverse radii a = 100 km, where each has a different peak disturbed ionospheric electron density profile (corresponding to profiles I, II, III, and IV of Figure 2). For comparison the figure shows the scattering pattern of the same mode (n = 3) for each case. (Other parameter values are f = 25 kHz, σ = 4 S/m, and ϵ_r = 81.) This result illustrates the fact that the effective angular width of the main lobe of the scattered radiation pattern is insensitive to differences in the ionospheric electron density profile of the disturbance. For this case, $\psi_{15} \cong 7^\circ$.

Figure 9 compares the relative magnitudes of the scattered radiation patterns of a typical waveguide mode (n = 5) for four disturbances of different effective radii (a = 25, 50, 100, and 200 km). Other parameter values for this example were taken to be f = 25 kHz, σ = 4 S/m, and ϵ_r = 81, and profile I of Figure 2 was assumed to represent the altitude variation of density at the center point. Notice that for disturbances which have radii of 50 km or larger, the scattered signal strength at $\psi = 20^\circ$ is lower by more than 40 dB with respect to the forward scattered signal strength. Even for the relatively small 25-km radius disturbance,

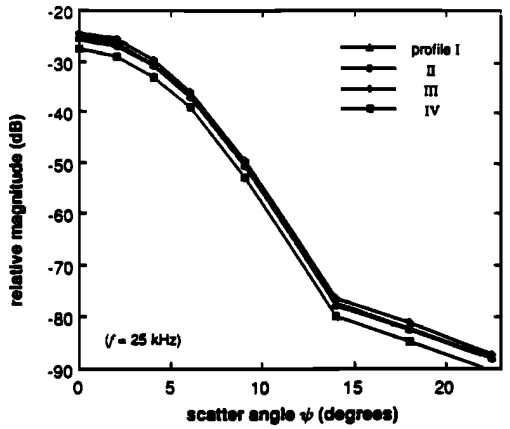

Fig. 8. Scattered modal strength versus ψ for different disturbed density profiles I, II, III, and IV as defined in Figure 2. All other parameters are the same as in Figure 6.

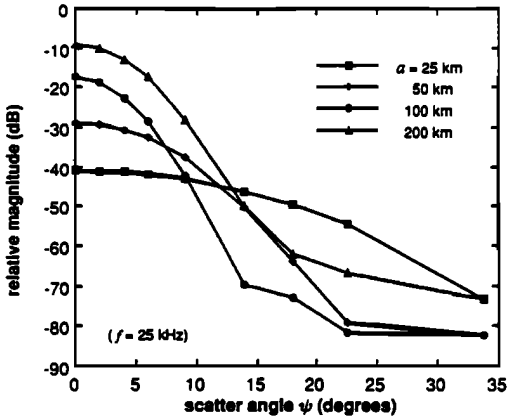

Fig. 9. Scattered modal signal strength versus ψ for disturbances of different sizes, with a = 25, 50, 100, and 200. Profile I of Figure 2 was assumed for the disturbance profile. All other parameters are the same as in Figure 6.

the scattered signal strength has diminished by more than 30 dB for scatter angles $\psi \geq 35°$. However, as can be seen for the forward scattered ($\psi = 0°$) signal strength, the smaller disturbances scatter a relatively smaller amount of signal than the larger disturbances (as measured by the comparison of scattering magnitudes at $\psi = 0°$). For example, the forward scatter for a 25 km radius is ~25 dB lower than for a 100-km radius and 11 dB lower than for a 50-km radius. Disturbances having radii smaller that 25 km were not considered, because such small disturbances begin to violate the WKB approximation used in this model. It also appears that the overall scattering effect of such small disturbances is lower, so that generally, much larger density changes would be needed to produce the same amplitude and phase changes at the receiver.

Since our calculations have concerned the particular density distribution given in (2), it is important to show that the radiation patterns we have presented in the figures are representative of those that would be produced by other distributions of enhanced density in the disturbed region. The Appendix considers two additional cases, namely, (1) a slowly varying localized disturbance which vanishes at the boundary where $f(r')=[1-(r'/a)^2]$ for $r \leq a$, and (2) a slowly varying more widespread disturbance where $f(r')=[1+4(r'/a)^2]^{-\frac{3}{2}}$ for $0 \leq r \leq \infty$.

In these cases, for f = 25 kHz and a = 50 km, the −15 dB beam width is shown to be in the range $\psi_{15} \sim 7°$-$8°$. Thus the results of Figure 9 for the Gaussian disturbance shape are within 40% of the results for these additional two cases, suggesting that the results shown in the figures are representative to this degree of accuracy.

The calculations in the Appendix are carried out under the assumption that $(\alpha a)^2 \ll 1$, where α is defined in (A4). At the midpoint of a 6000-km path with f=25 kHz, we have $\alpha=1.3\times10^{-2}$ km^{-1} and thus only the a = 25 km and a = 50 km plots of Figure 9 satisfy the condition $(\alpha a)^2 \ll 1$.

6. Summary And Discussion

We have shown that under fairly general conditions the VLF wave scattering produced in the Earth-ionosphere waveguide by a density enhancement perturbation in the lower ionosphere is predominantly independent of the conductivity and permittivity of the Earth's suface immediately beneath the perturbed region. The only exception to this rule is the case of extremely low conductivity such as could be found over the deep ice caps of Greenland and the Antarctic. This finding indicates that on midlatitude propagation paths the characteristics of the VLF wave scattered by an ionospheric disturbance depend primarily on the altitude distribution of density and the transverse shape of the disturbance. Thus it appears that the scattered signal can be used with confidence as a diagnostic tool to study the ionospheric disturbances.

Our results also indicate that for a 6000-km GCP and for the type of disturbances considered here, most of the measurable wave energy scatters within a fairly narrow angular region centered on the forward scatter direction. For the geometry shown in Figure 1 we can write $y_{15} = d \sin\psi_{15}/4$, where y_{15} is the lateral displacement of the perturbation from the GCP at which the amplitude of the scattered signal observed at the receiver is reduced by 15 dB below that in the forward scatter direction (ψ = 0). From Figure 9 it is seen that $\psi_{15} \sim 8°$ for f = 25 kHz and a = 100 km, and thus we have $y_{15} \cong$200 km.

For smaller values of a, assuming that $(a\alpha)^2 \ll 1$, we can use (A9) and (A10) to write $\psi \sim 4/ka$ and thus

$$y_{15} \cong d/ka \tag{4}$$

Equation (4) shows that the maximum displacement of the disturbed region is directly proportional to the length of the GCP connecting transmitter and receiver and inversely proportional to the phase shift across the horizontal extent of the disturbance (ka). For d = 6000 km, f = 25 kHz, and a = 50 km, $y_{15} \cong$ 250 km according to (4). Thus it is suggested that moderate- to large-scale disturbances ($50 \leq a \leq 200$ km) must be located within ~250 km of a moderate-scale GCP (3000-6000 km) in order to scatter a measurable signal to the receiver. This upper bound on y_{15} should aid in determining the exact location of the disturbed ionospheric region and the frequency of occurrence of those disturbances on a continent-wide scale [*Inan et al.*, 1990].

Equation (1) is derived assuming that each modal field satisfies the WKB approximation within the perturbed region [*Poulsen et al.*, 1990*a*]. When this approximation is satisfied, no significant mode coupling takes place and the input and scattered wave have similar mode structures. However, it is important to note that the WKB approximation may not be satisfied for ionospheric perturbations which either are larger than those of Figure 2 or occur over regions comparable to or smaller than one wavelength ($\leq$ 12 km for 25 kHz). In these cases, mode coupling may be important, and a different mathematical model is needed. Examples of cases in which such mode coupling is important are treated by *Wait* [1968; 1991*a*, *b*], *Pappert and Ferguson* [1986], and *Poulsen et*

al. [1990*b*]. In addition the WKB approximation can also fail in the case of degenerate eigenmodes where the eigenangles of two modes are very close in value [*J. R. Wait*, private communication]

APPENDIX: APPROXIMATE RADIATION PATTERNS OF SCATTERED WAVES

According to *Wait* [1964*a*], the approximate normalized wave field for each mode scattered by an ionospheric disturbance of limited horizontal extent can be expressed by the relation (the mode subscript n has been dropped in the following)

$$\frac{e^s}{e^o} = -(i)^{\frac{3}{2}} \frac{k_o \alpha}{\sqrt{\pi}} [S(0,0) - S^o] I \tag{A1}$$

where

$$I = \iint_{\mathcal{P}} f(x,y) e^{-i\alpha^2 y^2} dx dy \tag{A2}$$

$$f(x,y) = \frac{S(x,y) - S^o}{S(0,0) - S^o} \tag{A3}$$

$$\alpha = \left[k_o S^o \frac{d}{2 x_T x_R} \right]^{\frac{1}{2}} \tag{A4}$$

and where x and y are defined in Figure 1.

If we assume that $f(x,y)$ is cylindrically symmetric in the horizontal plane about the point (x_o, y_o) and that the observation point is located in the far field where $\alpha^2 a^2 \ll 1$, then we can express (A2) in the approximate form [*Wait*, 1964*b*]

$$I = 2\pi e^{-i\alpha^2 y_o^2} \int_0^a f(r) J_o(\eta r) r dr \tag{A5}$$

where $\eta = 2\alpha^2 y_o$, r is the radial (horizontal) distance from (x_o, y_o), J_o is the Bessel function of the first kind of order zero, and we have dropped the prime superscript from r. In general, η has a small imaginary part η_i, because S^o has a small imaginary part. If $\eta_i a \ll 1$, then η_i can be neglected in (A5). In the following we make this assumption.

The radiation pattern of the scattered wave can be found from (A1) and (A5) using the relations $y_o = R_o \sin\gamma = R' \sin\beta$, $x_T = R_o \cos\gamma$, $x_R = R' \cos\beta$, and $\psi = \gamma + \beta$, where R_o and R' are the fixed GCP distances between the center of the disturbed region and the transmitter and receiver, respectively, and γ and β are defined in Figure 1. For comparison with Figures 7-10, we assume that $R_o = R'$ and thus $\gamma = \beta = \frac{1}{2}\psi$ and $\alpha = \alpha(\psi) = [k_o S^o / R_o \cos(\psi/2)]^{\frac{1}{2}}$. Assuming that ψ is small, we see that $\alpha(\psi) \cong \alpha(\psi = 0) = \alpha_o$. Thus the radiation pattern of the scattered field can be simply expressed in terms of the forward scattered signal $e_s(\psi = 0) \equiv e_s(0)$:

$$P(\psi) = \left| \frac{e^s(\psi)}{e^s(0)} \right|^2 \simeq \left| \int_0^a f(r) J_o(\eta r) r dr \Big/ \int_0^a f(r) r dr \right|^2 \tag{A6}$$

where $\eta \cong k S_r^o \psi$ and S_r^o is the real part of S^o. It is worthy of note that the intensity distribution given in (A6) is similar to that obtaining in Fraunhofer diffraction of light through a circular aperture [*Born and Wolf*, 1965], where $f(r)$ represents the cylindrically symmetric distribution of wave amplitude across the aperture. If $f(r) > 0$, then it is clear from (A6) that the signal scattered towards an arbitrary angle ψ_o will always be less than that in the forward direction, since $|J_o(\eta r)| < 1$ for all $\eta r > 0$. Furthermore, the scattered signal should drop sharply for $\eta a \gg 1$, since in this case the term $J_o(\eta r)$ will have many periods in the integral of (A6) and the positive and negative portions will tend to cancel. For simplicity we can give a qualitative measure of the "beam width" of the radiation pattern as the angle ψ_B at which $\eta a \cong 2.4$. This is the first zero of $J_o(\eta a)$. Assuming $k a S_r^o \gg 1$,

$$\psi_B \sim 2.4 (k a S_r^o)^{-1} \tag{A7}$$

We note that ψ_B is inversely proportional to the total number of wavelengths across the scattering region. This is similar to the case of a uniform broadside antenna array [*Jordan and Balmain*, 1968].

The value of ψ_B given in (A7) is only a qualitative measure of beam width. To find quantitative values of ψ_B, we need to consider explicit models. For simplicity we consider only two models for $f(r)$:

model A	$f_A(r) = [1 - (\frac{r}{a})^2]$,	where $0 \le r \le a$
	$f_A(r) = 0$,	where $r > a$
model B	$f_B(r) = [1 + \frac{4r^2}{a^2}]^{-\frac{3}{2}}$,	where $0 \le r \le \infty$

The function $f_A(r)$ represents a localized ionospheric disturbance which varies slowly with r and vanishes at the boundary of the disturbed region. The function $f_B(r)$ represents a more widespread disturbance which varies slowly for $r < a$ but falls off quickly for $r > a$. These two functions have the same total amplitude within the disturbed region.

Insertion of $f_A(r)$ and $f_B(r)$ into (A6) yields the following results:

$$P_A(\psi) = [8 J_2(z)/z^2]^2 \tag{A8}$$

$$P_B(\psi) = e^{-z}$$

where $z = \eta a$.

The main lobe of $P_A(\psi)$ extends from the maximum value at $\psi = 0°$ to the first zero at $z \simeq \pm 5$. The secondary maxima in the pattern are more than 20 dB below the main lobe. The -15 dB bandwidth for this case occurs at the value $z \cong 4$, and thus the beam half angle is

$$|\psi_{15}^A| \approx 4/(ka) \tag{A9}$$

where we have set $S_r^o \cong 1$ for the lower-order modes.

For $f = 25$ kHz and $a = 50$ km, we find that $|\psi_{15}^A| \simeq 8°$. From Figure 9, for $a = 50$ km, it can be seen that the -15-dB point for mode 3 occurs at an angle of $\psi_{15} \simeq 12°$. Thus the -15-dB pattern for this case is roughly 70% as wide as that for the Gaussian perturbation.

For disturbance shape B the radiation pattern $P_B(\psi)$ consists of a single lobe. The -15-dB point occurs where $\gamma = 3.5$. For $f = 25$ kHz and $a = 50$ km, this relation yields

$$|\psi_{15}^B| \approx 7° \tag{A10}$$

Thus the main lobe of pattern $P_B(\psi)$ is roughly 60% as wide as that for the Gaussian perturbation shown in Figure 9.

Acknowledgments. This research was sponsored by the Office of Naval Research (ONR) under grant N00014-87-K-0299 to Stanford University. We greatly appreciate the interest in and support of this program by Gracen Joiner of ONR. The MODEFNDR program used to determine the mode refractive indices and the LWPC software were provided to us by J. A. Ferguson and F. P. Snyder of the Naval Ocean Systems Center (NOSC). We appreciate their support of this effort and our consultations with them on the use of the NOSC programs. We also appreciate discussions with our colleagues in the STAR Laboratory.

The Editor thanks J. R. Wait and another referee for their assistance in evaluating this paper.

REFERENCES

Born, M., and E. Wolf, *Principles of Optics*, Pergamon, New York, 1965.

Carpenter, D. L., U. S. Inan, M. L. Trimpi, R. A. Helliwell, and J. P. Katsufrakis, Perturbations of subionspheric LF and MF signals due to whistler-induced electron precipitation bursts, *J. Geophys. Res., 89*, 9857, 1984.

Chang, H. C., and U. S. Inan, Lightning induced energetic electron precipitation from the magnetosphere, *J. Geophys. Res., 90*, 1531, 1985.

Cotton, P. D., and A. J. Smith, The signature of burst particle precipitation on VLF signals propagating in the Antarctic, *J. Geophys. Res., 96*, 19,325, 1991.

Dowden, R. L., and C. D. D. Adams, Phase and amplitude perturbations on subionospheric signals explained in terms of echoes from lightning-induced electron precipitation ionization patches, *J. Geophys. Res., 93*, 11,543, 1988.

Dowden, R. L., and C. D. D. Adams, Phase and amplitude perturbations on the NWC signal at Dunedin from lightning-induced electron precipitation, *J. Geophys. Res., 94*, 497, 1989*a*.

Dowden, R. L., and C. D. D. Adams, Modal effects on amplitude perturbations on subionospheric signals (trimpis) deduced from two-frequency measurements, *J. Geophys. Res., 94*, 1515, 1989*b*.

Dowden, R. L., and C. D. D. Adams, Location of lightning-induced electron precipitation from measurement of VLF phase and amplitude perturbation on spaced antennas and on two frequencies, *J. Geophys. Res., 95*, 4135, 1990.

Hauser, J. P., W. E. Garner, and F. J. Rhoads, A VLF effective ground conductivity map of Canada and Greenland with revisions derived from propagation data, *NRL Rep. 6893*, Naval Res. Lab., Washington, D. C., March 1969.

Helliwell, R. A., J. P. Katsufrakis, and M. L. Trimpi, Whistler-induced amplitude perturbation in VLF propagation, *J. Geophys. Res., 78*, 4679, 1973.

Inan, U. S., and D. L. Carpenter, Lightning-induced electron precipitation events observed at $L \sim 2.4$ as phase and amplitude perturbations on subionospheric VLF signals, *J. Geophys. Res., 92*, 3293, 1987.

Inan, U. S., W. C. Burgess, T. G. Wolf, D. C. Shafer, and R. E. Orville, Lightning-associated precipitation of MeV electrons from the inner radiation belt, *Geophys. Res. Lett., 15*, 172, 1988*a*.

Inan, U. S., T. G. Wolf, and D. L. Carpenter, Geographic distribution of lightning-induced electron precipitation observed as VLF/LF perturbation events, *J. Geophys. Res., 93*, 9841, 1988*b*.

Inan, U. S., F. A. Knifsend, and J. Oh, Subionospheric VLF "imaging" of lightning-induced electron precipitation from the magnetosphere, *J. Geophys. Res., 95*, 17217, 1990.

Jordan, E. C., and K. G. Balmain, *Electromagnetic Waves and Radiating Systems*, p. 364, Prentice-Hall, Englewood Cliffs, N. J., 1968.

Lohrey, B., and A. B. Kaiser, Whistler-induced anomalies in VLF propagation, *J. Geophys. Res., 84*, 5121, 1979.

Pappert, R. A., and J. A. Ferguson, VLF/LF mode conversion model calculations for air to air transmission in the Earth-ionosphere waveguide, *Radio Sci., 21*, 551, 1986.

Poulsen, W. L., T. F. Bell, and U. S. Inan, Three-dimensional modeling of subionospheric VLF propagation in the presence of localized *D* region perturbations associated with lightning, *J. Geophys. Res., 95*, 2355, 1990*a*.

Poulsen, W. L., T. F. Bell, and U. S. Inan, Subionospheric VLF signal variations due to strong D-region perturbations caused by precipitating energetic electrons, *Eos Trans. AGU, 71(43)*, 1535, 1990*b*.

Poulsen, W. L., U. S. Inan, and T. F. Bell, A multiple-mode three-dimensional model of VLF propagation in the earth-ionosphere waveguide in the presence of localized D region disturbances, *J. Geophys. Res., 98*, No. A2, 1705-1717, 1993.

Wait, J. R., An analysis of VLF mode propagation for a variable ionosphere height, *J. Res. Natl. Bur. Stand., Sect. D, 66*, 453, 1962.

Wait, J. R., Calculated diffraction effects at VLF from a localized ionospheric depression, *Tech. Note 208*, Natl. Bur. of Stand., Boulder, Colo., 1964*a*.

Wait, J. R., On phase changes in very-low-frequency propagation induced by an ionospheric depression of finite extent, *J. Geophys. Res., 69*, 441, 1964*b*.

Wait, J. R., Mode conversion and refraction effects in the earth-ionosphere waveguide for VLF radio waves, *J. Geophys. Res., 73*, 3537, 1968.

Wait, J. R., EM scattering from a vertical column of ionization in the Earth-ionosphere wave guide, *IEEE Trans. Antennas Propag., 39*, 1051, 1991*a*.

Wait, J. R., VLF radio wave mode conversion for ionospheric depressions, *Radio Sci., 26*, 1261, 1991*b*.

Wolf, T. G., and U. S. Inan, Path-dependent properties of subionospheric VLF amplitude and phase perturbations associated with lightning, *J. Geophys. Res., 95*, 20,997, 1990.

Yip, W.-Y., U. S. Inan, and R. E. Orville, On the spatial relationship between lightning discharges and propagation paths of perturbed subionospheric VLF/LF signals, *J. Geophys. Res., 96*, 249, 1991.

T. F. Bell, and U. S. Inan, STAR Laboratory, Department of Electrical Engineering, Stanford University, Stanford, CA 94305-4055.

W. L. Poulsen, Jet Propulsion Laboratory, Mail Stop 300-319, 4800 Oak Grove Drive, Pasadena, CA 91109.

(Received May 8, 1992;
revised March 9, 1993;
accepted April 16, 1993.)